Soft Matter

PAPER

View Article Online
View Journal | View Issue

Cite this: *Soft Matter*, 2025, **21**, 1686

Temperature dependence of phase diagrams and dynamics in nanocrystal assembly by solvent evaporation†

Alex Upah, [a] Leandro Missoni, [b] Mario Tagliazucchi *[b] and Alex Travesset *[a]

We provide a systematic study of the phase diagram and dynamics for single component nanocrystals (NCs) by a combination of a self-consistent mean-field molecular theory (MOLT-CF) and molecular dynamics (MD) simulations. We first compute several thermodynamic functions (free energy, entropy, coefficient of thermal expansion and bulk modulus) as a function of temperature by both MOLT-CF and MD. While MOLT-CF correctly captures the trends with temperature, the predicted coefficients of thermal expansion and bulk moduli display quantitative deviations from MD and experiments, which we trace back to the mean-field treatment of attractions in MOLT-CF. We further characterize the phase diagram and calculate the dependence on temperature of the bcc to fcc transition. Our results reveal that differences in entropic and enthalpic contributions to the free energy oscillate as a function of NC separation and are correlated to a geometric quantity: the volume of overlap between the ligand layers in different particles. In this way, we generally show that bcc is favored by enthalpy, while fcc is by entropy, in agreement with previous experimental evidence of fcc stabilization with increasing temperature, but contrary to what is expected from simpler particle models, where bcc is always entropically favored. We also show that the lowest relaxation times drastically increase in the latest stages of solvent evaporation. Overall, our results demonstrate that MOLT-CF provides an adequate quantitative model describing all phenomenology in single component NCs.

Received 29th October 2024,
Accepted 23rd January 2025

DOI: 10.1039/d4sm01265h

rsc.li/soft-matter-journal

1 Introduction

Assembly of nanocrystals (NCs) into ordered arrays provides a route to engineering materials with structures and properties that are inaccessible with more traditional building blocks such as atoms and molecules. In this context, assembly by solvent evaporation has become one of the most robust strategies for the engineering of nanostructures.[1,2] The goal of this paper is to provide a detailed characterization of the thermodynamic properties of single-component superlattices (SLs) at different stages of the solvent evaporation process, with a particular emphasis on the role of temperature, as well as a general description of the dynamics. For this purpose, we use MOLT-CF (molecular theory for compressible fluids) and molecular dynamics (MD) simulations. Recent experimental advances[3] provide the ability to halt the evaporation process at any intermediate state and, in this way, characterize the structure of any possible activation or metastable state, thus making it possible to rigorously verify the predictions presented in this paper.

In a previous paper[4] we introduced MOLT-CF by extending previous models[5,6] as a general predictive tool for both structure and dynamics. We verified MOLT-CF with MD simulations and demonstrated that it successfully predicts the available experimental phenomenology in single-component superlattices (SLs), including the fcc-to-bcc transition as a function of the length of the hydrocarbon ligands for dry systems[7,8] and the fcc-to-bcc Bain transition as a function of decreasing solvent content.[9–11] We also showed that MOLT-CF satisfies an incompressibility condition (IC), which implies that the ligands and solvent fill out 3D space with constant density. In fact, the IC alone can be used to predict many aspects of the structure, such as lattice constants.[12]

In our first study[4] only a single temperature was investigated. Yet, there are many important effects related to temperature. In ref. 13, it was shown that an interplay between the solvent and the ligand leads to a complex non-linear

[a] *Department of Physics and Astronomy, Iowa State University and Ames National Laboratory, Ames, Iowa 50011, USA. E-mail: trvsst@ameslab.gov*
[b] *Departamento de Química Inorgánica Analítica y Química Física, Ciudad Universitaria, Facultad de Ciencias Exactas y Naturales, Universidad de Buenos Aires, Pabellón 2 C1428EGA, Buenos Aires, Argentina*

† Electronic supplementary information (ESI) available: Contains technical details of the calculations and additional plots complementing the ones in the main paper. See DOI: https://doi.org/10.1039/d4sm01265h

agglomeration as a function of temperature. Temperature plays an important role in determining the phase diagram of SLs. For example, in binary systems[14] many different SL phases are observed in the temperature range between 253 K and 358 K. Furthermore, temperature provides a powerful knob to develop reconfigurable materials as demonstrated by the recently developed thermally triggerable ligands.[15] Oleate capped NCs show that increasing temperature leads to a reversible bcc → bct → fcc transition,[16,17] which strongly suggests that the entropy of fcc is larger than that of bcc, $S_{fcc} > S_{bcc}$. This conclusion is supported by isothermal microcalorimetry measurements (with PbSe cores), which have shown that bcc has a lower enthalpy than fcc (*i.e.*, bcc is favoured by energy).[18] Goodfellow *et al.*[19] used Gaussian-chain statistics to determine ligand entropy, which predicts $S_{fcc} < S_{bcc}$, in disagreement with the considerations above. On the other hand, MD simulations by Fan and Grünwald[20] have shown that the bcc–fcc entropy difference oscillates with the softness parameter λ ($\lambda = 2L/D_c$, where D_c is the core diameter and L is the ligand length): entropy favours fcc for $0.56 < \lambda < 0.98$, but it disfavours this phase for $\lambda < 0.56$ or $\lambda > 0.98$. As a comparison, the experiments referred above[16–18] correspond to $\lambda \sim 0.57$–0.89. These results paint a rather nuanced picture of the thermodynamics of the bcc–fcc phase transition in SLs.

A critical aspect for high-quality assembly of materials is the characterization of the longest relaxation time τ_R. If the experimental (or simulation) time t is shorter than τ_R, different modes within the system remain out of equilibrium, and the quality of assembly decreases. Simulations reported in ref. 21 and 22 provided evidence that in the latest stages of evaporation, τ_R is inversely proportional to the solvent diffusion coefficient, which in turn becomes vanishingly small as the solvent diffuses by a mechanism of hopping from one ligand to the next. Yet, these conclusions were obtained from simulations that only considered clusters with a small number of NCs. In this paper, we extend these results by describing how solvent diffusion takes place in SLs and analyze its temperature dependence.

The paper is organized as follows: we first describe general aspects of MOLT-CF and simulations, and then present the results: first fundamental thermodynamic quantities and then the phase diagram, with particular emphasis on the bcc–fcc critical region. We also analyze the dependence on the enthalpic and entropic components of the free energy and finalize with the determination of relaxation times. We complete the paper with a summary and general conclusions. We also discuss the applicability of MOLT-CF to broader systems.

2 General aspects of theory and simulation

2.1 Definition of the system

We consider n_c quasi-spherical NPs, *i.e.* truncated octahedra for simulations and some MOLT-CF calculations, and spherical in other MOLT-CF calculations. We therefore characterize the NC core by its diameter D_c, grafted with n_l ligands containing $n_{h,l}$ monomers each. There are also n_s solvent molecules, each consisting of $n_{h,s}$ monomers.

The n_c NCs are positioned in the corresponding SL sites, either holding them with springs in the simulation or simply fixing the positions within MOLT-CF. Then, thermodynamic functions such as the Helmholtz free energy $F(T,V,n_c,n_s)$ are obtained as a function of lattice constant (or volume).

The NCs are surrounded by the solvent, and if the lattice constant is sufficiently large, there is additional free space separating the NCs in different lattice sites. As the lattice parameter is reduced, the solvent eventually condenses and fills the entire space not occupied by the NCs, as discussed in our previous paper.[4]

2.2 The incompressibility condition

The IC is the statement that solvent and NC fill the entire space, and it is precisely formulated as

$$V = \frac{\pi}{6} D_c^3 n_c + n_{h,l} n_l n_c \upsilon_l + n_{h,s} n_s \upsilon_s \tag{1}$$

where $\upsilon_{l/s}$ are the molecular volumes for ligand and solvent monomers respectively. Even if both ligands and solvent consist of the same type of monomer, alkane chains for example, as it is considered in this paper, it must be assumed that $\upsilon_l \neq \upsilon_s$. This is because at high grafting densities the ligand monomers, specially close to the core, are subject to large forces, resulting in a much reduced molecular volume. Therefore, we expect that $\upsilon_l < \upsilon_s$. The IC in a SL is stated as

$$V_{UC} = n_{UC}^{SL} \left(\frac{\pi}{6} D_c^3 + n_{h,l} n_l \upsilon_l + \frac{n_s}{n_c} n_{h,s} \upsilon_s \right) \tag{2}$$

where V_{UC} is the volume and n_{UC}^{SL} the number of NCs within a unit cell. Using the cubic bcc/fcc unit cells, then $V_{UC} = a_L^3$ and $n_{UC}^{SL} = 2/4$, respectively. The formula for the nearest-neighbor d follows as

$$d = \left\{ \begin{array}{c} \left(\frac{3}{4}\sqrt{3}\right)^{1/3} \\ \\ \left(\sqrt{2}\right)^{1/3} \end{array} \right\} \left(\frac{\pi}{6} D_c^3 + n_{h,l} n_l \upsilon_l + \frac{n_s}{n_c} n_{h,s} \upsilon_s \right)^{1/3} \tag{3}$$

where the top result corresponds to bcc and the bottom to fcc. Of course, for this formula to have real predictive value, both υ_l and υ_s need to be obtained from independent calculations not involving an SL.

Following previous work we define the solvent fraction as

$$\Phi_s = \frac{n_{h,s} n_s \upsilon_s}{V}. \tag{4}$$

and it is convenient to introduce the ligand Φ_l and core Φ_c volume fractions as

$$\begin{array}{c} \Phi_l = \dfrac{n_{h,s} n_l n_c \upsilon_l}{V} \\ \\ \Phi_c = \dfrac{\pi D^3 n_c}{6V} \end{array} \quad \text{with } \Phi_s + \Phi_l + \Phi_c = 1, \tag{5}$$

where the last equality requires that there are no voids, *i.e.* the entire volume is occupied by NCs and solvent in the liquid

state. The actual volume occupied by matter can be approximated as[12]

$$V_{\text{matter}} = \frac{\pi}{6} D_c^3 n_c + n_h L_l A_{0,l} + n_s L_s A_{0,s} \tag{6}$$

where $L_{l/s}$ is the maximum extent of the ligand/solvent and $A_{0,l/s}$ is its footprint (or molecular area). Basically, these formulas assume that ligand/solvent molecules have an intrinsic volume = $A_{0,l/s}L_{l/s}$. This volume is different to (and smaller than) $n_{h,l/s}\upsilon_{l/s}$, as the latter is a measure of the free volume and includes the available space where the molecules vibrate, while the former defines the actual volume occupied by matter. In other words, $A_{0,l/s}L_{l/s}$ has a meaning similar to a van der Waals molecular volume, while $n_{h,l/s}\upsilon_{l/s}$ is analogous to a partial molecular volume. Therefore the packing fraction is given as

$$\eta_{\text{HS}} = \frac{V_{\text{matter}}}{V} = \frac{\frac{\pi}{6} D_c^3 n_c + n_l L_l A_{0,l} + n_s L_s A_{0,s}}{V}. \tag{7}$$

For a dry system without voids, $n_s = 0$ and the above formula, combined with eqn (1) gives an explicit expression for υ_l

$$\upsilon_l = \left(\frac{1}{\eta_{\text{HS}}} - 1\right)\frac{\pi D^3}{6 n_{h,l} n_l} + \frac{L_l A_0}{n_{h,l}\eta_{\text{HS}}}. \tag{8}$$

With the currently accepted values for A_0,L and with $\eta_{\text{HS}} = \frac{\pi}{6}\sqrt{2} \approx 0.7405$, as extensively discussed in ref. 12 υ_l is unambigously determined. An independent simulation of the pure solvent determines υ_s

$$\begin{aligned} \upsilon_l\ (T/\text{K} = 387,\ 300) &= 28.5,\ 28.5\ \text{Å}^3 \\ \upsilon_s\ (T/\text{K} = 387,\ 300) &= 39.5,\ 34.8\ \text{Å}^3 \end{aligned} \tag{9}$$

As expected, $\upsilon_l < \upsilon_s$. The simulation and experimental results at $T = 298.15$ K reported in ref. 23 are respectively $\upsilon_s = 35.3$ Å^3 and $\upsilon_s = 36.3$ Å^3. There is a clear temperature dependence for υ_s, but υ_l is less sensitive to the temperature because the monomers are subjected to large forces and are therefore much less sensitive to k_BT variations.

Because the molecular volume depends on temperature, the values of Φ_s in eqn (4) for a fixed number of solvent molecules change slightly as a function of temperature. We will label the system by the value at Φ_s at $T = 387$ K and quote their values at other temperatures.

2.3 Dynamical scales in solvent evaporation

Ref. 21 and 22 show that the slowest relaxation time τ_R in a solvent evaporation process is given as

$$\tau_R \approx \frac{V^{2/3}}{D} \tag{10}$$

When the solvent is the majority component, V is the volume of the entire system, basically the volume of the vapor phase, and D is the diffusion constant of the vapor. This model amounts to the well known Maxwell model for evaporation.[24] In the latest stages of the evaporation process, defined by the NC occupying about 50% of the available volume, with the other 50% occupied by the solvent in the liquid phase, D_l is the solvent diffusion coefficient and V the volume of the NC–solvent mixture, so eqn (10) becomes

$$\tau_R \approx \frac{V_l^{2/3}}{D_l} \propto \frac{n_c^{2/3}}{D_l}, \tag{11}$$

which shows that the relaxation times are inversely proportional to the diffusion constant. Here D_l is much smaller than the Stokes–Einstein value $D_{\text{SE}} \propto \frac{k_B T}{R\eta}$ (R, η solvent radius and viscosity) characterizing the pure solvent, as the solvent residing mainly in the interstitial lattice needs to diffuse through the ligands by hopping from one NC to the next, until it eventually reaches the boundary of the system and escapes into the vapor phase.

2.4 Some technical aspects regarding simulations

We performed molecular dynamics (MD) simulations using HOODLT,[25] which runs HOOMD-Blue[26] with rigid body dynamics[27] with the opls force field.[23] We simulate temperatures in the range 305–387 K. Fig. 1 illustrates how a typical simulation proceeds.

The simulations were all done with $Au_{1072}(SC_{12})_{229}$, which is a gold core grafted with $n_l = 229$ dodecanethiol ligands ($n_{h,l} = 12$). The diameter of the core is $D = 3.53$ nm, resulting in a grafting density $\sigma = 5.85$ chains per nm^2, the same reported

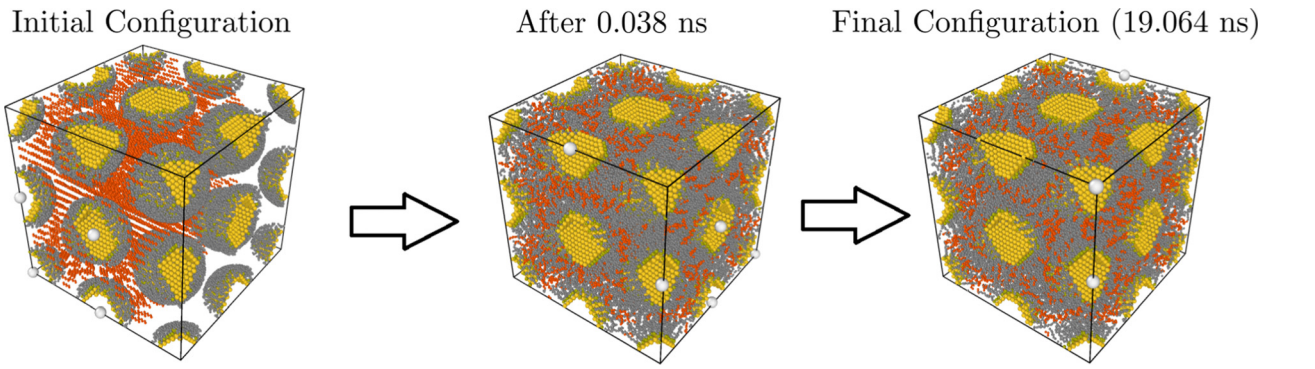

Fig. 1 Summary of a typical simulation: a bcc configuration with $a_L = 63$ Å and $\Phi_v = 0.18$. The solvent (hexane) is marked in red. In the left there is the initial configuration, which after only 0.381 ns is roughly thermalized. The configuration at the end of the simulation (19.064 ns) is shown.

in our previous papers.[4,28] The results in this paper make a clear case that free energies and any other thermodynamical quantities calculated from MOLT-CF are transferable to any other NC.

The free energy is calculated by computing the reversible work as outlined in our previous papers.[4,28,29] The diffusion constants are obtained by a fit to the relation

$$\langle((\vec{r}(t) - \vec{r}(t=0))^2\rangle = 6Dt \quad \text{for large } t \tag{12}$$

after removing periodic boundary conditions by particle images.

2.5 Some technical aspects regarding MOLT-CF calculations

The model used is the same described in ref. 4. Briefly, MOLT-CF is based on writing down and minimizing the free-energy functional of the system, Ω, which is canonical for the particle cores and ligands and grand-canonical for the solvent molecules. Ω contains the following contributions:

$$\beta\Omega[T,V,n_{\mathrm{UC}}^{\mathrm{SL}},\mu_{\mathrm{s}}] = \beta F_{\mathrm{Tr,s}} + \beta F_{\mathrm{Conf}} + \beta F_{\mathrm{vdW}} + \beta F_{\mathrm{HS}} - \beta\mu_{\mathrm{s}} n_{\mathrm{s}} \tag{13}$$

$\beta F_{\mathrm{Tr,s}}$ and βF_{Conf} are the free energies due to the entropies of solvent translation and solvent and ligand conformational freedom. βF_{vdW} models the vdW attractions ($\sim r^{-6}$) between the CH_2/CH_3 beads in the ligands and solvent. βF_{HS} is a position-dependent hard-sphere functional that accounts for bead–bead repulsions. Finally, $-\beta\mu_{\mathrm{s}} n_{\mathrm{s}}$ is included because Ω is a grand canonical potential for the solvent (n_{s} and μ_{s} are the number and chemical potential of solvent molecules, respectively). In the dry limit, this term is absent and Ω is equal to the total Helmholtz free energy, F. As explained in the ESI† and ref. 4, Ω depends on functions that describe the structure of the system in three-dimensions and are *a priori* unknown. The functional minimization of Ω with respect to those functions results in a set of self-consistent equations that are discretized and solved using numerical methods. As an output, we obtain structural and thermodynamical information of the system.

Ω takes as an input a set of conformations of the ligands and solvent molecules and, therefore, the theory explicitly takes into account the molecular details of those molecules. While previous formulations of the molecular theory (MOLT) employed a packing constraint and a good-solvent approximation to model hard-core repulsions and attractive forces,[5,6,30] MOLT-CF explicitly models these contributions with a hard-sphere (HS) functional (βF_{HS}) and a mean-field van der Waals attraction (βF_{vdW}), respectively. This modification enables modelling of both dry and solvent-containing SLs[5] and allows deviations from IC. A succinct description is provided in ESI† for completeness.

3 Results

3.1 Thermodynamic functions

Fig. 2a shows the free energy predicted by MD at T = 387 K (similar plots for other temperatures are provided in ESI†) for different amounts of solvent.

The dry case free energy is shown in Fig. 2b. The depth of the potential becomes larger with decreasing temperature, as the absolute value of the cohesive energy increases relative to $k_{\mathrm{B}}T$. Swollen systems, see Fig. 2c and d, follow similar trends to the dry case but display a stronger temperature dependence of the lattice constant. The agreement with the IC eqn (3), using the molecular volumes in eqn (9), is excellent.

Simulations are compared against MOLT-CF predictions in Fig. 3a for the equilibrium (minimum) free energy and in Fig. 3b for the lattice constant. Qualitatively, both results follow the same trends, with lattice constants and free energies decreasing with temperature. There is a small but significant deviation between MOLT-CF and MD, parameterized by the coefficient of thermal expansion

$$\begin{aligned}\alpha &= \frac{1}{V}\left(\frac{\partial V}{\partial T}\right)_{P,n_{\mathrm{c}},n_{\mathrm{s}}} \\ &= 3\left(\frac{\partial}{\partial T}\log(a_{\mathrm{l}})\right)_{P,n_{\mathrm{c}},n_{\mathrm{s}}} \\ &\approx \Phi_{\mathrm{s}}\left(\frac{\partial}{\partial T}\log(\upsilon_{\mathrm{s}})\right)_{P,n_{\mathrm{c}},n_{\mathrm{s}}} + \Phi_{\mathrm{l}}\left(\frac{\partial}{\partial T}\log(\upsilon_{\mathrm{l}})\right)_{P,n_{\mathrm{c}},n_{\mathrm{s}}},\end{aligned} \tag{14}$$

Within MD, the thermal expansion coefficient for the inorganic core is zero as the core is modeled as a rigid body. Experimentally, it is found that the thermal expansion coefficient of the core $\alpha_{\mathrm{PbS}}(300\ \mathrm{K}) = 2 \times 10^{-5}\ \mathrm{K}^{-1}$ (ref. 31) is two orders of magnitude smaller than that of the organic component $\alpha_{n\text{-hexane}}(300\ \mathrm{K}) = 1.5 \times 10^{-3}\ \mathrm{K}^{-1}$,[32] so assuming $\alpha \approx 0$ for the NC core is a well-justified approximation. MD provides α values in good agreement with the experiment, see Table 1 and a more detailed comparison in ESI.†

Table 1 summarizes the coefficient of thermal expansion predicted by MOLT-CF and MD and measured experimentally. MOLT-CF overestimates α compared with MD and experiments (for liquid *n*-hexane), which in turn, explains the small discrepancy between lattice constants and equilibrium free energies in Fig. 3a and b.

The experimental thermal expansion coefficient was estimated from Fig. 1 in ref. 34 by using the formula

$$\alpha \approx 3\frac{\log(a_{\mathrm{L}}(T_{\max})/a_{\mathrm{l}}(T_{\min}))}{T_{\max} - T_{\min}} \tag{15}$$

and corresponds to NPs with D_{c} = 3.6 nm and dodecanethiol ligands, very close to the system studied here. It is obtained from the peaks of the structure factor using the formula $a_{\mathrm{L,bcc}} = 2\pi\sqrt{2}/q$. If the interval between T/K = [313.15,363.15] is used, then $\alpha < 0.0005\ \mathrm{K}^{-1}$, but $\alpha \approx 0.0005\ \mathrm{K}^{-1}$ between T/K = [363.15,413.15]. Ref. 16 measured $\alpha = 1.2 \times 10^{-4}\ \mathrm{K}^{-1}$ at T = 300 K, consistent with these estimates.

It is also of interest to examine the bulk modulus B and the isothermal compressibility κ

$$B = \frac{1}{\kappa} = -V\left(\frac{\partial P}{\partial V}\right)_{\mathrm{T}} = V\left(\frac{\partial^2 F}{\partial V^2}\right)_{\mathrm{T}}. \tag{16}$$

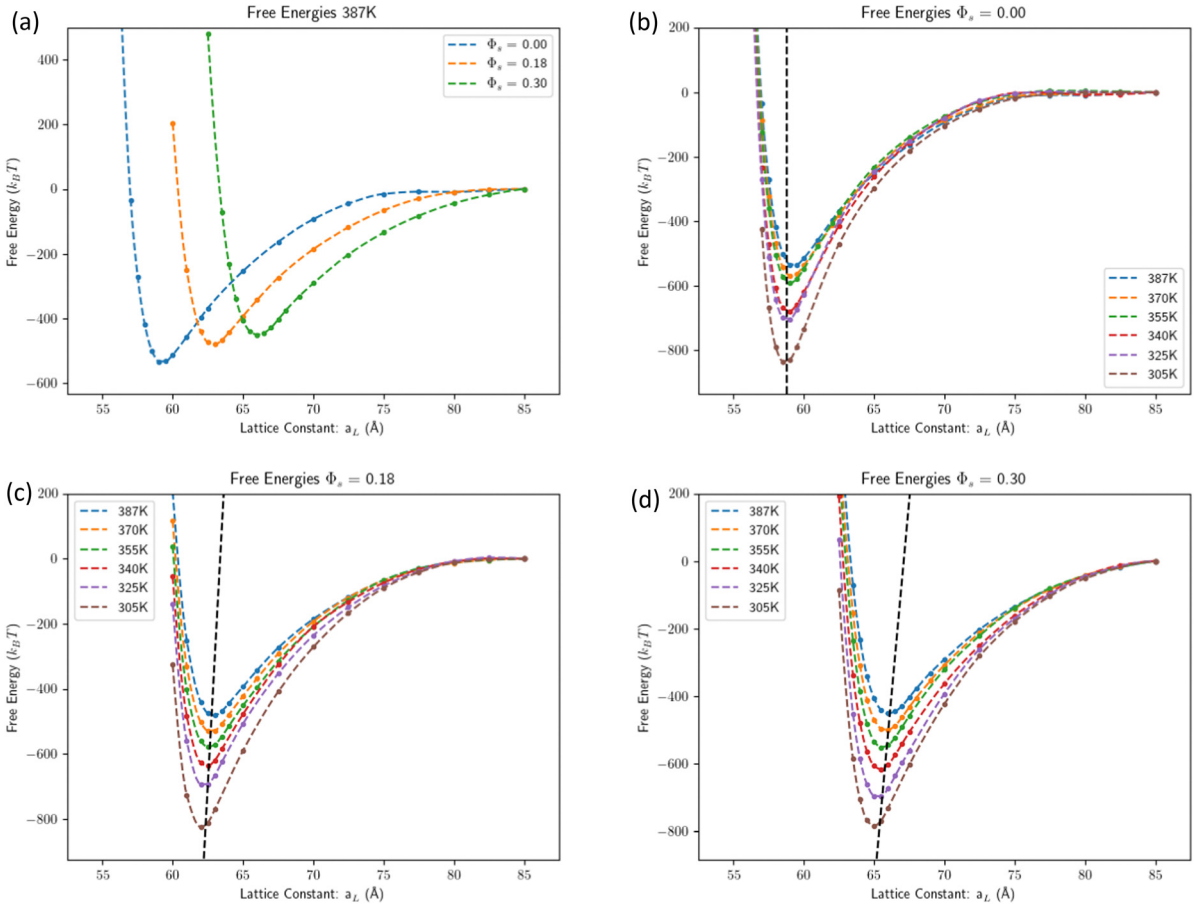

Fig. 2 Free energies computed by MD. (a) Free energy at T = 387 K predicted by MD for the three solvent contents considered. (b) Free energy predicted by MD for Φ_v = 0 (dry case) at all simulated temperatures. The dashed lines are the predictions from eqn (9) with the molecular volumes from eqn (9). (c) Free energy predicted by MD for Φ_s = 0.18 at all simulated temperatures. (Because of the temperature dependence of the molecular volume eqn (9) it is $\Phi_s(T = 387) = 0.180$ $\Phi_s(T = 305) = 0.162$ approximated as $\Phi_s = 0.18$.) (d) Free energy predicted by MD for Φ_s = 0.298 at all temperatures simulated. (Because of the temperature dependence of the molecular volume eqn (9) it is $\Phi_s(T = 387) = 0.298$ $\Phi_s(T = 305) = 0.274$ approximated as $\Phi_s = 0.30$.)

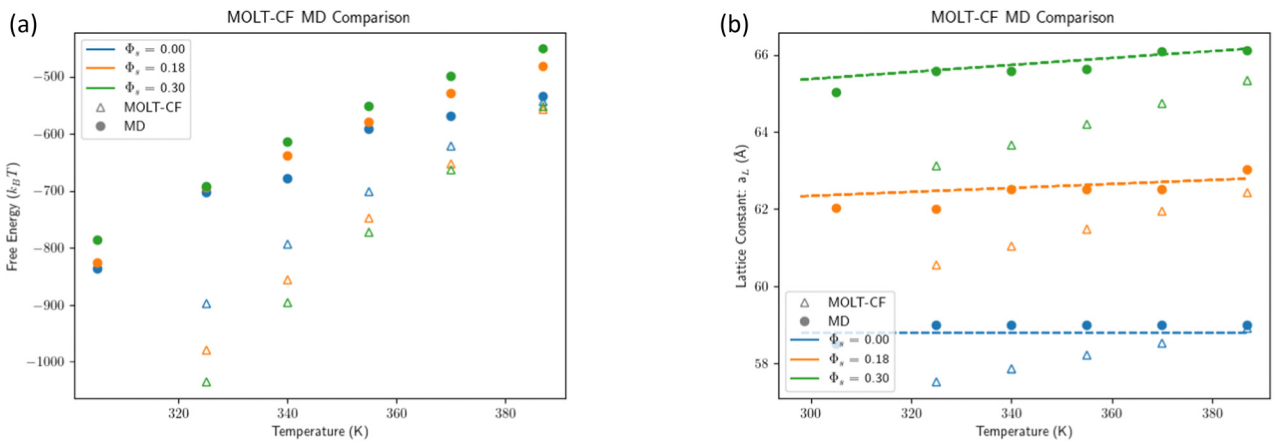

Fig. 3 Comparison of MOLT-CF *vs.* simulation. (a) Comparison of the free energy minimum computed with MOLT-CF and MD simulations. (b) Comparison of lattice constant MOLT-CF and MD simulations. The dashed lines illustrate the prediction eqn (3) with the molecular volume eqn (9).

Table 1 Thermal coefficient expansion, α/K^{-1}. * means estimated using eqn (15) as a function of the number of solvent molecules per unit cell, where in parenthesis we quote the value of Φ_s at T = 387 K. More detailed results for pure hexane are provided in ESI. Experimental results are for hexane are from ref. 32 and 33

Method	Dry(0)	1496(0.18)	2912(0.3)	Liq. hexane (300 K)
MOLT-CF	0.0011	0.0015	0.0017	0.0037
MD	0.0004	0.0005	0.0005	0.0013(1)
Exp.	~0.0001			0.0014

Table 2 Temperature dependence of bulk modulus B (GPa) and lattice constant a_L (nm) as a function of the number of solvent molecules per unit cell, where in parenthesis we quote the value of Φ_s at T = 387 K, as parameterized by eqn (18)

Quantity	Dry(0.0)	1496(0.18)	2912(0.3)
B_L(305 K)	6.0	5.4	3.5
c_B	0.027	0.025	0.015
a_L(305 K)	58.5	61.8	64.8
c_L	0.008	0.01	0.01

Within MD, we compute the bulk modulus at the minimum of the free energy from the equation

$$P = -B\frac{V - V_{min}}{V_{min}} = -B\frac{V}{V_{min}} + B \quad (17)$$

where V_{min} is the volume at the free energy minimum. The intercept provides the bulk modulus B, and the slope of the fit an accurate estimate for the lattice constant at the minimum. We parameterize the results according to

$$B(T) = B(T = 305) - (T - 305)c_B \quad (18)$$

$$a_L(T) = a_L(T = 305) + (T - 305)c_a, \quad (19)$$

with actual coefficients given in Table 2. Note that this value for the lattice constant provides a self-consistent accurate determination of the coefficient of linear expansion, and for this reason, is the value quoted in Table 1. We should mention, however, that fitting to eqn (17) is susceptible to large errors and consequently, relatively low precision estimates. In ESI† information we discuss how the results are actually obtained from the simulation and show some examples for the fits. Higher precision determinations for B would require calculations that are beyond the goals of this paper.

As shown in Fig. 4, B decreases with T for both MOLT-CF and MD, but MOLT-CF underestimates the bulk modulus when compared against MD. Experimental results give a value of the order $B \approx 5$ GPa[35] entirely consistent with MD. Overall, there is a small but significant temperature dependence on B, getting smaller with increasing temperature, reflected by the negative sign of the slope in eqn (18). We mention the MOLT-CF prediction of B for liquid hexane ($B_{MOLT\text{-}CF}$ = 203 MPa at P = 1 MPa and T = 387 K), which is also smaller than the experimental value in the same conditions ($B_{Experiment}$ = 352 MPa[36]).

3.2 Phase boundaries

Fig. 5a summarizes MOLT-CF predictions in the dry limit (for a core diameter D_c = 3.53 nm) as a function of ligand length $n_{h,l}$ and temperature. This transition is expected to take place at[8]

$$L^{crit} \approx \lambda_c \frac{D_c}{2} \Rightarrow n_{h,l}^{crit} \approx 8 \quad (20)$$

where the critical softness is λ_c = 0.7 and the maximum ligand length is given by the formula L/nm = 0.128$n_{h,l}$ + 0.2.[12] Fig. 5a predicts that $n_{h,l}^{crit}$ is temperature dependent. The breakdown of the different contributions to the bcc–fcc free energy difference is given in Fig. 5b. The free energy due to the ligands entropy ($\beta F_{conf} = -S_{conf}/k_B$) favors fcc ($F_{conf}$(bcc) > F_{conf}(fcc)). On the other hand, the energy of ligand–ligand interactions (vdW attractions + HS repulsions) favors bcc. Finally, the energy of the *gauche*/*trans* dihedral angles favors bcc, but its contribution is rather small.

The fact that fcc is favored by entropy (S_{conf}(fcc) > S_{conf}(bcc)) and bcc by energy results in the prediction of a bcc → fcc transition for increasing T (Fig. 6), in agreement with experimental observations for oleate capped PbS NPs.[16,17]

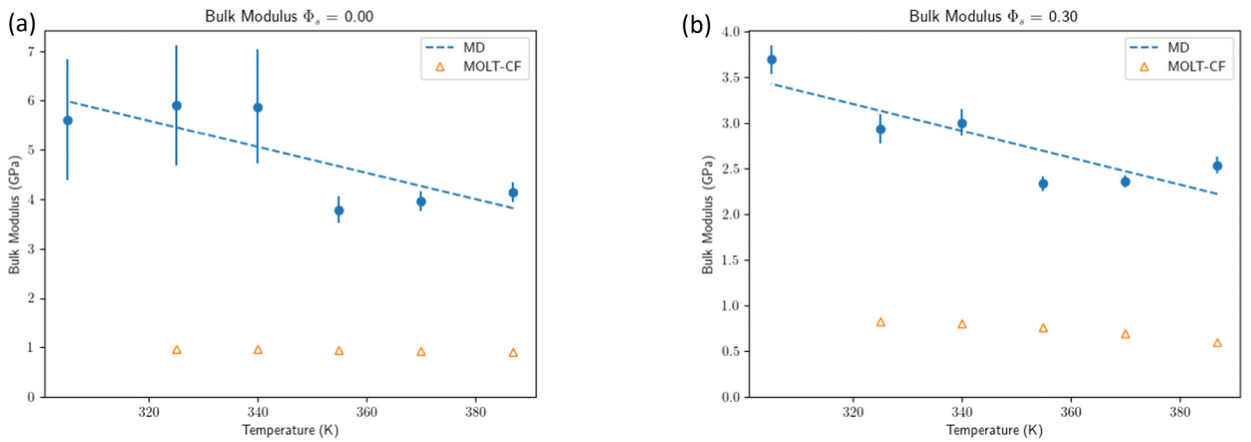

Fig. 4 Comparison of bulk modulus eqn (16) MOLT-CF *vs.* MD simulations. See the ESI† for additional plots and a more elaborated discussion. (a) Bulk modulus for the dry system. (b) Bulk modulus for the swollen system.

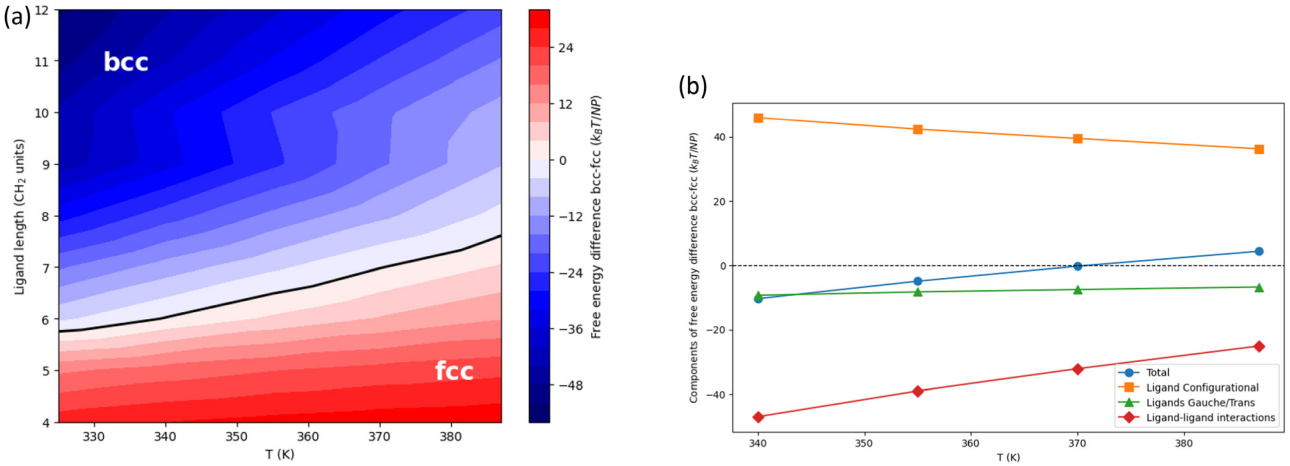

Fig. 5 Bcc *vs.* fcc stability in the dry case. (a) Free energy difference between bcc and fcc for the dry system predicted by MOLT-CF. (b) Contributions to the free energy difference between bcc and fcc for the dry system and $n_{h,l}$ = 7 predicted by MOLT-CF.

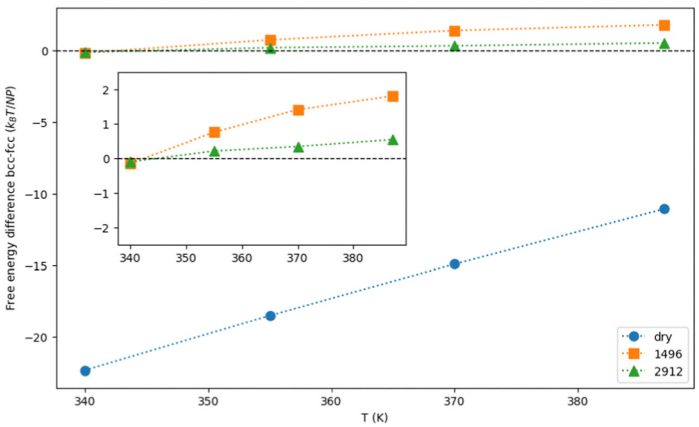

Fig. 6 Free energy difference between bcc and fcc for the $n_{h,l}$ = 12 and different solvent contents predicted by MOLT-CF.

3.3 Origin of the bcc–fcc transition

Fig. 7 shows the entropic (ligand conformations, solid red lines) and energetic (vdW + HS + *gauche*, dashed red lines) contributions to the bcc–fcc Helmholtz free-energy difference in the dry limit (with spherical cores) as a function of the average NC particle distance

$$\bar{d} = (V_{UC}/n_{UC}^{SL})^{1/3}. \quad (21)$$

Note that $\bar{d}^3$ is the volume per NP, $\frac{V}{n_c}$, and therefore, the value of $\bar{d}$ is different for each lattice.

The equilibrium $\bar{d}_{eq}$ (minimum of F) is approximately given by the IC condition (see above), and it is indicated with vertical dashed lines in Fig. 7. The different contributions to the bcc–fcc free-energy difference, $\Delta_{bcc-fcc}F_j$, oscillate as a function of $\bar{d}$. Interestingly, similar oscillations were observed by Fan *et al.*[20] for $\Delta_{bcc-fcc}S$ and $\Delta_{bcc-fcc}U$ (obtained by MD simulations) *vs.* the softness parameter λ, as well as in the different contributions of the free energy *vs.* solvent content in our previous model for SLs using a packing constraint.[5]

We now define the overlap volume $V_{overlap}$ (see the inset in Fig. 7) of two NCs of radius $R = \frac{D_c}{2}$ and ligand shell h. More precisely, taking a test NC at the origin, then

$$V_{overlap} = \int_R^{R+h} r^2 dr \int_0^{2\pi} d\theta \int_0^{\pi} d(\cos(\phi)) M(r,\theta,\phi), \quad (22)$$

where the function $M(r,\theta,\phi)$ is 1 if at the point $\mathbf{r} = (r,\theta,\phi)$ there is an overlapping ligand shell or core of a particle (different than the test particle) or 0 otherwise.

$$M(\mathbf{r}) = 1 - \prod_j \vartheta\left(|\mathbf{r} - \mathbf{r}_j| - (R+h)\right), \quad (23)$$

where ϑ is the Heaviside step function and the product runs over all particles in the SL different from the test particle, which are located at positions $\mathbf{r}_j$. As expected, $V_{overlap}$ monotonically decreases with increasing $\bar{d}$, reaching zero for large $\bar{d}$ and becoming equal to the volume of the ligand shell at very small $\bar{d}$ (not shown).

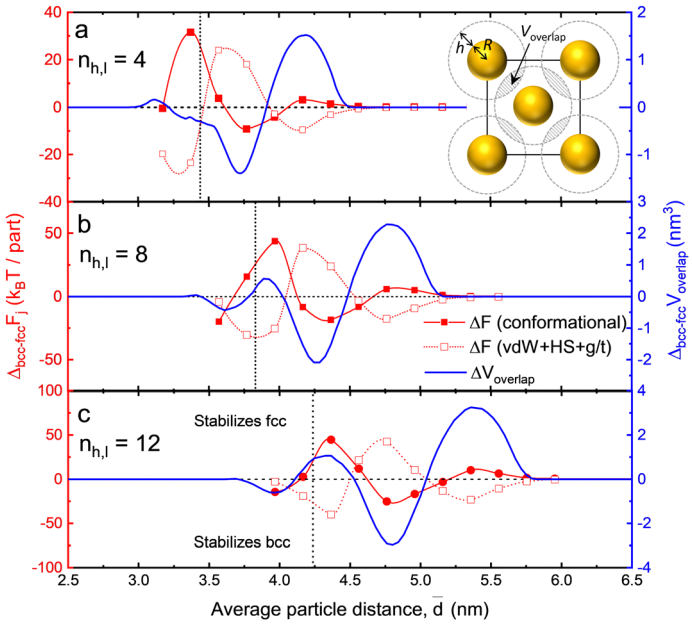

Fig. 7 (a)–(c) Difference between the ligad–shell overlap volume in bcc and fcc lattices (blue line, see inset in panel (a)) and free-energy contributions due to ligand entropy (red solid lines and filled symbols) and energy (red dotted lines and empty symbols) *vs.* average distance per particle, $(V_{UC}/n_{UC}^{SL})^{1/3}$, for a dry SL of 1.5-nm radii spherical NPs coated by ligands of 4 (a), 8 (b) and 12 (c) C per chain at T = 387 K. The equilibrium volumes per NP (corresponding to the minima of the free energy) are indicated with black dotted vertical lines. The free energy is calculated by MOLT-CF.

The difference $\Delta_{bcc-fcc}V_{overlap}$ (blue line in Fig. 7) oscillates as a function of $\bar{d}$. For $\bar{d} \to \infty$, both overlap volumes are zero, so $\Delta_{bcc-fcc}V_{overlap} = 0$. As the NCs approach, $\Delta_{bcc-fcc}V_{overlap}$ first becomes positive because the nearest neighbors in bcc are closer than in fcc (Table 3). As $\bar{d}$ continues to decrease, the sign of $\Delta_{bcc-fcc}V_{overlap}$ reverses because fcc has more nearest neighbors than bcc. $\Delta_{bcc-fcc}V_{overlap}$ displays additional oscillations due to the differences in the distance and numbers of nearest and next to nearest neighbors in both phases, until it becomes zero again in the limit of small $\bar{d}$, where the overlap volumes of both phases become equal to the volume of the ligand shell.

If $\Delta_{bcc-fcc}V_{overlap} > 0$, then there is more ligand overlap in bcc than fcc, and intuitively, both the internal energy and entropy should be expected to be lower for bcc than fcc. Fig. 7 shows that this is exactly what is found, with $\Delta_{bcc-fcc}F$(conformational) $\approx -T\Delta S$(entropy) anti-correlated to $\Delta_{bcc-fcc}F$(vdW + HS + g/t) $\approx \Delta_{bcc-fcc}U$(enthalpy).

The key parameter in the definition of $V_{overlap}$ is the ligand shell h. A first estimate would consider h as the maximum extended size of the ligand, which is proportional to the softness λ

$$h \approx L_l = (0.128n_{h,l} + 0.2)\ \text{nm} = R\lambda = \frac{D_c}{2}\lambda \qquad (24)$$

see eqn (20) and (21). A slightly more precise definition considers instead the size of the NC in vacuum using

$$h = a(n_{h,l} + 1) + b, \qquad (25)$$

The constant a = 0.088 nm results from fitting MOLT-CF calculations for an isolated NC, and b = 0.525 nm represents the range of the vdW attractions. The difference between eqn (24) and (25) is numerically small.

The largest $\bar{d} = \bar{d}_{max}$ where the overlap difference is different from zero is

$$2(R + h) \approx c\bar{d}_{max} \to \frac{\bar{d}_{max}}{R + h} = \frac{2}{c} \approx 1.8 \qquad (26)$$

where $c = 2^{\frac{1}{6}}$ is obtained from the value for fcc in eqn (3). Therefore, the new dimensionless variable

$$u \equiv \frac{\bar{d}}{R + h} \qquad (27)$$

is such that the maximum value where volume overlap is different from zero is $u_{max} \approx 1.8$ independent of ligand length and NC core diameter.

Fig. 8a–c shows the free energies and overlap differences as a function of u. From previous considerations, the equilibrium value, *i.e.* the one determined by the incompressibility

Table 3 Number and distance of nearest neighbors (NN) and next-nearest neighbors (NNN) in bcc and fcc lattices

Cell	Type	Distance/$\bar{d}$	Number
bcc	NN	$2^{-2/3} \times 3^{1/2} = 1.09$	8
fcc	NN	$2^{1/6} = 1.12$	12
bcc	NNN	$2^{1/3} = 1.26$	6
fcc	NNN	$2^{2/3} = 1.59$	6

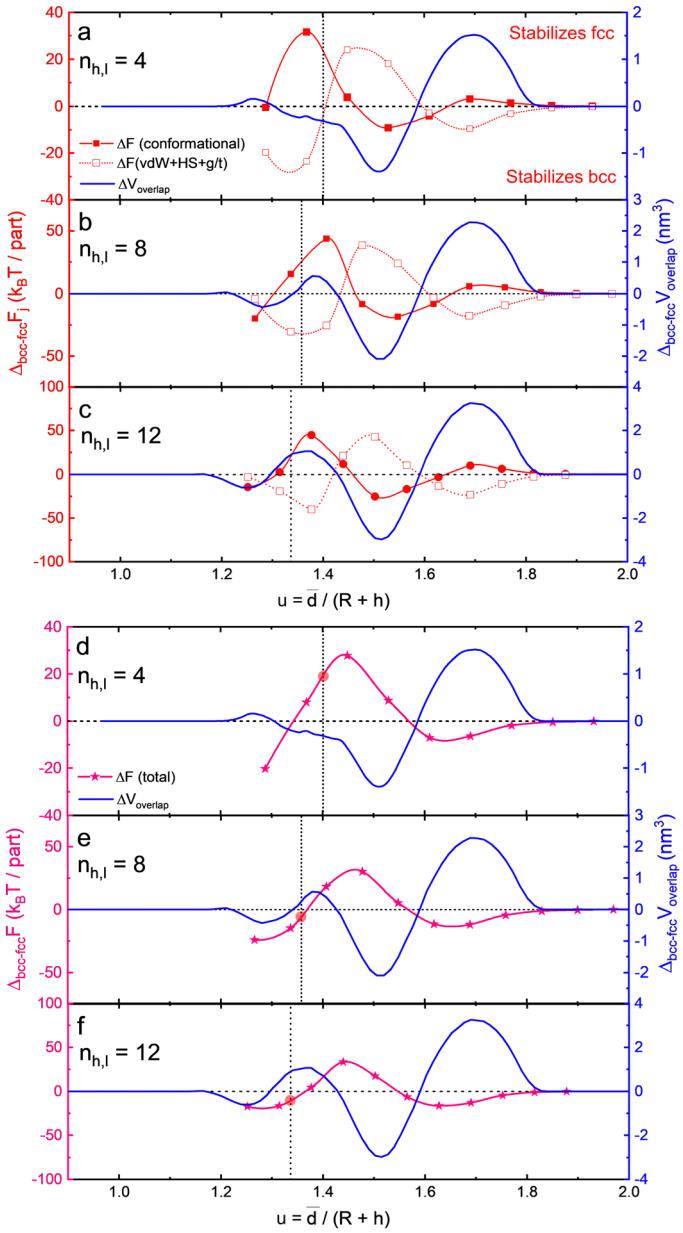

Fig. 8 Top panel: (a)–(c) Same as Fig. 7 but rescaling the average particle distance by the total particle size, $R + h$. (d)–(f) Bottom panel: Same as (a)–(c) but with the total bcc–fcc free energy difference. The free energy is calculated by MOLT-CF.

condition is approximately given by

$$u_{eq} = \frac{\bar{d}_{eq}}{R+h} \approx 2\left(\frac{\pi}{6}\right)^{1/3} \frac{\left(1 + 3\lambda\xi\frac{\upsilon_s}{A_0 b}\right)^{1/3}}{1+\lambda}, \qquad (28)$$

where we used eqn (2) and $\lambda = \frac{2L_l}{D_c}$ is the softness and $\xi = \sigma A_0$ the dimensionless grafting density, see eqn (6) for the definition of the other parameters. For large values of $n_{h,l}$ ($\lambda \gg 1$), eqn (28) implies that u_{eq} shifts to the left for increasing softness as $u_{eq} \propto \lambda^{-2/3}$.

Fig. 8d–f shows the total free-energy differences as a function of u. As expected from the discussion in the previous paragraph, $u_{max} \approx 1.8$. Eqn (28) predicts that u_{eq} (position of the vertical dashed line in Fig. 8) shifts to the left as the ligand becomes longer (λ becomes larger): $u_{eq} = 1.55$, 1.45, and 1.35 for $n = 4$, 8, and 12. Fig. 8d–f shows that increasing the ligand length (increasing λ) decreases u_{eq}, which for the approximately universal $\Delta_{bcc-fcc}F$ *vs.* u curve shown in magenta lines, increases the stability of the bcc phase, in good agreement with previous theoretical and experimental works.[4,5,20,29,37,38]

3.4 Dynamics

The data obtained from MD simulations will now be used to characterize the dynamics of the system. Because diffusion coefficients are dynamical quantities, they cannot be compared

Table 4 Experimental *vs.* predicted diffusion coefficients of *n*-hexane, D_l ($m^2\ s^{-1}$)

T/K	Experiment	MD simulation
387		10.4×10^{-9}
333	6.0×10^{-9}	6.7×10^{-9}
305	4.2×10^{-9}	4.8×10^{-9}

with MOLT-CF. Yet, they are still important for an appropriate characterization of the system. The slowest relaxation time of a SL as the solvent evaporates, see eqn (10), is directly related to the solvent diffusion coefficient, D_l, and its dependence on solvent volume fraction Φ_s, see also eqn (11). Therefore, we consider first the diffusion coefficient for pure solvent, *i.e.* hexane, and then present a detailed analysis of its dependence within an SL.

The diffusion coefficients reported in ref. 39 for pure *n*-hexane are compared against our MD predictions, Table 4.

We then performed two types of simulations. In the first case, see Fig. 11, we consider a bcc SL with a fixed number of hexane molecules per cubic unit cell n^s_{UC}, with the two cases n^s_{UC} = 187 and 364 explicitly simulated. If the lattice constant a_L is large, there are voids in the system, as apparent in the largest constant in Fig. 11, and some of the solvent molecules are in the gas phase. In Fig. 9a we show the diffusion coefficient, computed according to eqn (12), as a function of the lattice constant at T = 387 K. At large lattice constants there are significant voids and diffusion is fast D_l/D_l(hexane) $\gg$ 1. As the lattice constant reaches its equilibrium value, the diffusion constant is significantly below the magnitude of D_l(hexane). Fig. 9b and c show the dependence of the diffusion coefficient on temperature and a_L. As expected, D_l increases with temperature and with the number of solvent molecules.

The second type of simulation consists of NC separated by a lattice constant a_L, where the remaining box is completely filled with the solvent. These simulations enable the determination of $D_l(\Phi_s)$ for any Φ_s, including the limit $\Phi_s \to 1$, where the diffusion coefficient should reach the pure solvent D_l(hexane) value. Results are shown in Fig. 10. At large solvent fractions, D approaches D_l(hexane) but as the solvent is further evaporated D/D_l(hexane) $\ll$ 1 because the solvent resides primarily in interstitial lattice sites[4] and the ligands act as "obstacles"

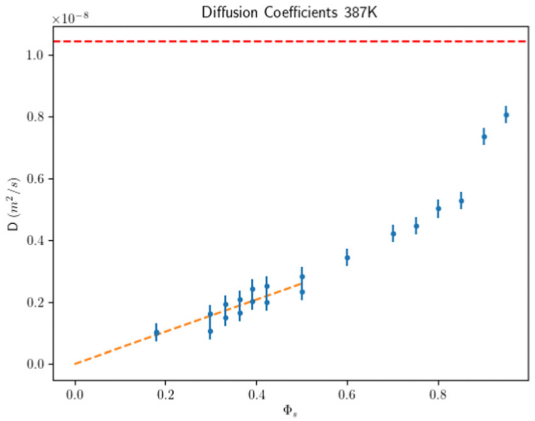

Fig. 10 Hexane diffusion coefficient from MD simulations as a function of Φ_v at the minimum of the free energy for T = 387. The dashed red line is the diffusion coefficient for hexane. The dashed orange fit shows that the limit of the diffusion at a low volume fraction is consistent with zero.

which drastically reduce the diffusion coefficient. A fit for small solvent volume fractions shows that D_l extrapolates to zero at $\Phi_s \to 0$, see Fig. 10. In the ESI† we provide similar plots for other temperatures, which exhibit the same trends.

4 Conclusions

We have provided a detailed account of the thermodynamics and dynamics of assembly by solvent evaporation as a function of temperature. Our results show that MOLT-CF[4] generally agrees well with simulations albeit with small but significant quantitative discrepancies (except, perhaps, for the elastic constants). The simulations presented, in turn, are in agreement with the experimental results.

The quantitative discrepancies between MOLT-CF and the simulations are traced back to the fact that MOLT-CF overestimates the coefficient of thermal expansion α and underestimates the bulk modulus B. We recall that MOLT-CF models interbead interactions as a combination of a hard-sphere potential and an algebraic attraction of the form r^{-6}. The former is modeled using a position-dependent Carnahan–Starling functional and the latter is taken into account at the mean-field level. For homogeneous fluids, this combination is

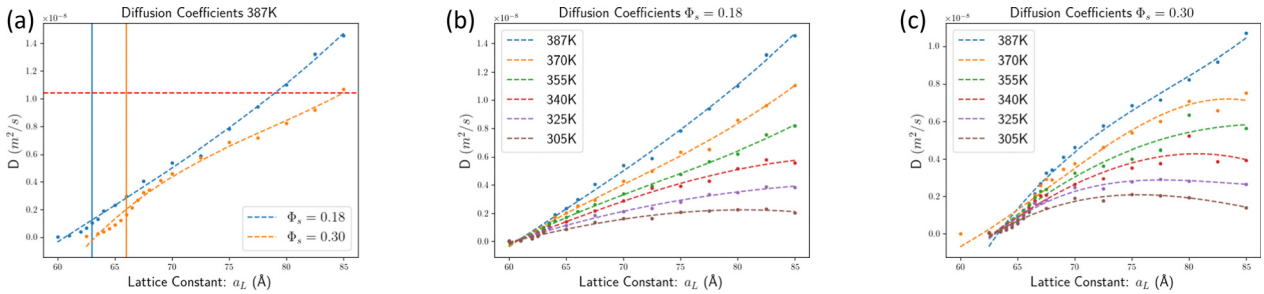

Fig. 9 Values of diffusion coefficients from MD simulations. (a) Diffusion constants at T = 387 K as a function of lattice constant. The vertical lines are the lattice constants at the two solvent concentrations. (b) Diffusion coefficient for different temperatures for $\Phi_v \approx 0.18$. (c) Diffusion coefficient for different temperatures for $\Phi_v \approx 0.3$.

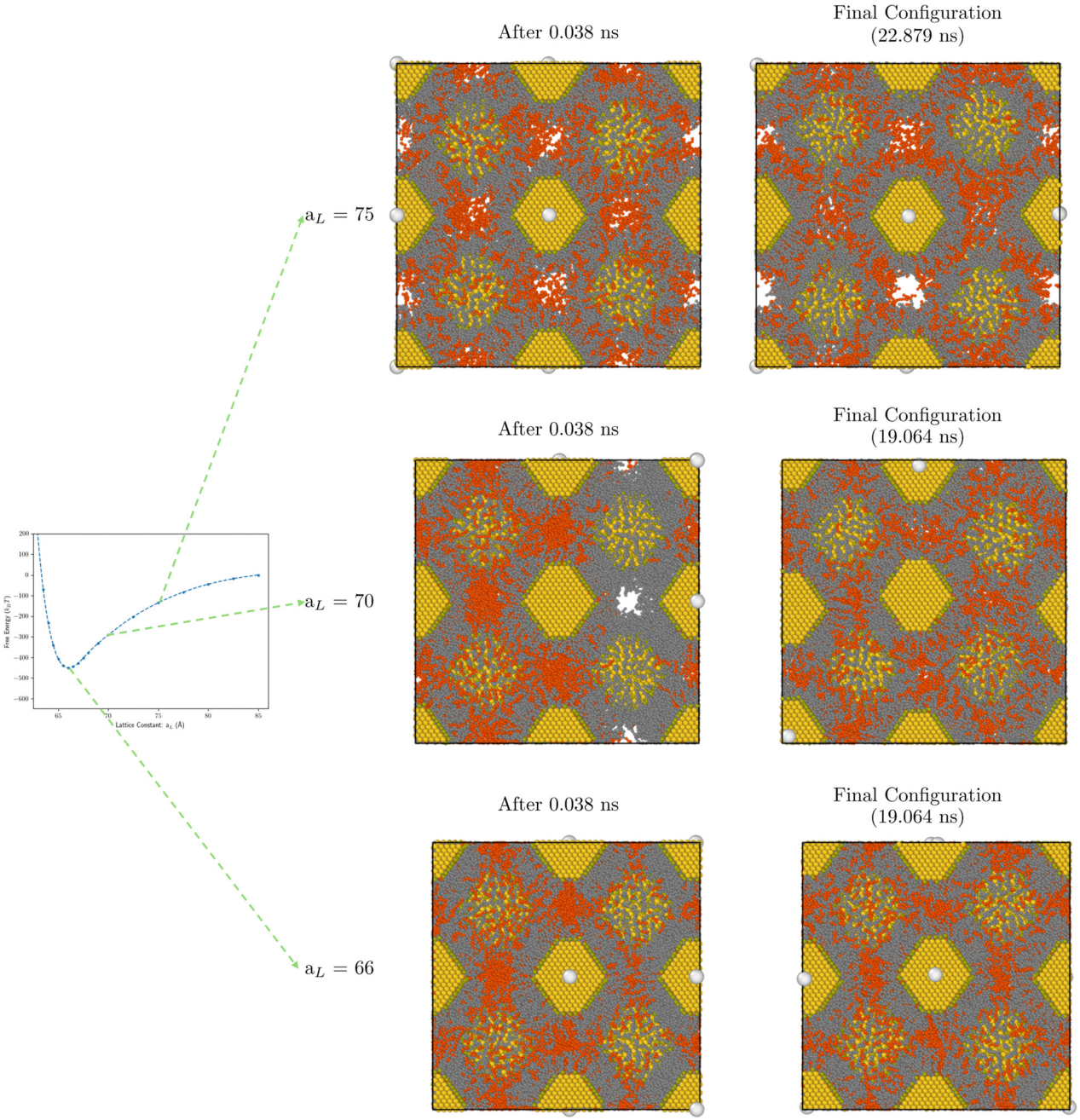

Fig. 11 Visualization of bcc configurations with Φ_v = 0.30 at increasing a_L at 0.038 ns and 19.064 ns in MD simulation.

known as the augmented van der Waals theory,[40] which has the advantages of being simple and physically intuitive and of requiring only two fitting parameters, but certainly ignores relevant correlations.[41] It should be possible to include more complex functionals that improve the accuracy of the thermal expansion coefficient and the bulk modulus. However, our results show that MOLT-CF describes the equilibrium lattice constant and free-energy minimum at 387 K in very good agreement with MD simulations. This excellent level of agreement is observed because MOLT-CF was originally parameterized to reproduce the density of the hexane and NC ligands at 387 K and P close to P_{vap} (0.33 MPa). An alternative approach is possible without modifying the functional form and consists of parameterizing MOLT-CF with temperature-dependent coefficients so that the solvent phase diagram quantitatively agrees with simulations and experiments. In this way, the model has no predictive power with regard to the solvent, but still remains fully predictive for the prediction of the stable phases in nanoparticle systems.

MOLT-CF very generally shows that fcc is favored by entropy while bcc by enthalpy. This is a somewhat counterintuitive result: calculations that treat ligands implicitly by using soft

interparticle interaction potentials[25] show that the vibrational (phonon) entropy of bcc is always larger than fcc, a result that is attributed to the slightly more spherical bcc-shell. For the same reason, polymer theory considering ideal Gaussian statistics[19] also predicts that bcc is entropically favored. We have provided a physical interpretation of the bcc to fcc transition by examining how the entropic and enthalpic components change as a function of NC separation; see Fig. 7, and have shown that entropy and energy differences between bcc and fcc are strongly correlated to a purely geometric quantity: the difference in volume overlap eqn (22), thus underlying a universal description, *i.e.* holding true for a large class of NC interactions irrespective of actual microscopic details.

It was shown in ref. 21 and 22 that the slowest relaxation time is inversely proportional to the solvent diffusion coefficient. Our simulations show that the diffusion coefficient consistently vanishes as the solvent content tends to zero, implying a significant slowdown in the latest stages of the evaporation process.

In summary, we have provided a detailed investigation of the thermodynamic properties, phase behavior and relaxation timescales of NC single component systems. For the former two sets of properties, MOLT-CF provides a powerful self-consistent theory that favorably compares with experimental results and MD predictions.

The success of MOLT-CF in predicting all the available phenomenology in single component systems, makes a strong case for its applicability in more general cases. Indeed, with minor modifications to the calculations presented in this paper, this tool can be applied to any NC shape, for example, ref. 42 and 43, multicomponent NC systems[12,44] and other cases, such as patchy NCs.[45] We will definitely report on this in the near future.

Author contributions

AT and MT designed the project. AU performed MD and MT and LM performed the MOLT-CF calculations. All authors participated in the data analysis. AT and MT wrote the paper.

Data availability

The data used in this paper are available free of charge at the DataShare repository at Iowa State University **https://www.lib.iastate.edu/collections/datashare-isu-data-repository** with the digital object identifier: **https://doi.org/10.25380/iastate.27879912**.

Conflicts of interest

There are no conflicts to declare.

Acknowledgements

AT acknowledges interest and discussions with S. Mallapragada and D. Vaknin and X. Ye. AT and AU work is supported by NSF-DMR-CMMT 2402548. MT is a fellow of CONICET. MT acknowledges financial support from ANPCyT (PICT 1520-2019) and CONICET (PIP 11220200102008C). This work used EXPANSE and BRIDGES2 through allocation MCB140071 from the Advanced Cyberinfrastructure Coordination Ecosystem: Services Support (ACCESS) program,[46] which is supported by National Science Foundation grants 2138259, 2138286, 2138307, 2137603, and 2138296.

Notes and references

1 C. L. Bassani, G. van Anders, U. Banin, D. Baranov, Q. Chen, M. Dijkstra, M. S. Dimitriyev, E. Efrati, J. Faraudo, O. Gang, N. Gaston, R. Golestanian, G. I. Guerrero-Garcia, M. Gruenwald, A. Haji-Akbari, M. Ibáñez, M. Karg, T. Kraus, B. Lee, R. C. Van Lehn, R. J. Macfarlane, B. M. Mognetti, A. Nikoubashman, S. Osat, O. V. Prezhdo, G. M. Rotskoff, L. Saiz, A.-C. Shi, S. Skrabalak, I. I. Smalyukh, M. Tagliazucchi, D. V. Talapin, A. V. Tkachenko, S. Tretiak, D. Vaknin, A. Widmer-Cooper, G. C. L. Wong, X. Ye, S. Zhou, E. Rabani, M. Engel and A. Travesset, *ACS Nano*, 2024, **18**, 14791–14840.
2 M. A. Boles, M. Engel and D. V. Talapin, *Chem. Rev.*, 2016, **116**, 11220–11289.
3 Y. Wang, J. Chen, C. Zhu, B. Zhu, S. Jeong, Y. Yi, Y. Liu, J. Fiadorwu, P. He and X. Ye, *Nano Lett.*, 2021, **21**, 5053–5059.
4 L. L. Missoni, A. Upah, G. Zaldívar, A. Travesset and M. Tagliazucchi, *Nano Lett.*, 2024, **24**, 5270–5276.
5 L. L. Missoni and M. Tagliazucchi, *ACS Nano*, 2020, **14**, 5649–5658.
6 L. Missoni and M. Tagliazucchi, *Nanoscale*, 2021, **13**, 14371–14381.
7 R. L. Whetten, M. N. Shafigullin, J. T. Khoury, T. G. Schaaff, I. Vezmar, M. M. Alvarez and A. Wilkinson, *Acc. Chem. Res.*, 1999, **32**, 397–406.
8 U. Landman and W. D. Luedtke, *Faraday Discuss.*, 2004, **125**, 1–22.
9 K. Bian, J. J. Choi, A. Kaushik, P. Clancy, D.-M. M. Smilgies and T. Hanrath, *ACS Nano*, 2011, **5**, 2815–2823.
10 M. C. Weidman, D.-M. M. Smilgies and W. A. Tisdale, *Nat. Mater.*, 2016, **15**, 775–781.
11 I. Lokteva, M. Koof, M. Walther, G. Grübel and F. Lehmkühler, *Small*, 2019, **15**, 1900438.
12 A. Travesset, *Curr. Opin. Solid State Mater. Sci.*, 2024, **30**, 101159.
13 M. R. Hasan, B.-J. Niebuur, M. Siebrecht, B. Kuttich, R. Schweins, A. Widmer-Cooper and T. Kraus, *ACS Nano*, 2023, **17**, 9302–9312.
14 M. I. Bodnarchuk, M. V. Kovalenko, W. Heiss and D. V. Talapin, *J. Am. Chem. Soc.*, 2010, **132**, 11967–11977.
15 Y. Ning, S. Yang, D.-B. Yang, Y.-Y. Cai, J. Xu, R. Li, Y. Zhang, C. R. Kagan, J. G. Saven and C. B. Murray, *J. Am. Chem. Soc.*, 2024, **146**, 3785–3795.

16 R. H. Gilmore, S. W. Winslow, E. M. Y. Lee, M. N. Ashner, K. G. Yager, A. P. Willard and W. A. Tisdale, *ACS Nano*, 2018, **12**, 7741–7749.
17 S. W. Winslow, D.-M. Smilgies, J. W. Swan and W. A. Tisdale, *J. Phys. Chem. C*, 2020, **124**, 13456–13466.
18 Z. Quan, H. Xu, C. Wang, X. Wen, Y. Wang, J. Zhu, R. Li, C. J. Sheehan, Z. Wang, D.-M. Smilgies, Z. Luo and J. Fang, *J. Am. Chem. Soc.*, 2014, **136**, 1352–1359.
19 B. W. Goodfellow, Y. Yu, C. A. Bosoy, D.-M. Smilgies and B. A. Korgel, *J. Phys. Chem. Lett.*, 2015, **6**, 2406–2412.
20 Z. Fan and M. Gruenwald, *ChemRxiv*, 2019, preprint, DOI: 10.26434/chemrxiv.9178037.v1.
21 E. Macias, T. Waltmann and A. Travesset, *Soft Matter*, 2020, **16**, 7350–7358.
22 T. Waltmann and A. Travesset, *Nanoscale*, 2019, **11**, 18702–18714.
23 W. L. Jorgensen, J. D. Madura and C. J. Swenson, *J. Am. Chem. Soc.*, 1984, **106**, 6638–6646.
24 N. Fuchs, *Evaporation and Droplet Growth In Gaseous Media*, Pergamon Press, 1st edn, 1959, pp. 1–72.
25 A. Travesset, *J. Chem. Phys.*, 2014, **141**, 164501.
26 J. A. Anderson, C. D. Lorenz and A. Travesset, *J. Comput. Phys.*, 2008, **227**, 5342–5359.
27 T. D. Nguyen, C. L. Phillips, J. A. Anderson and S. C. Glotzer, *Comput. Phys. Commun.*, 2011, **182**, 2307–2313.
28 A. Upah, A. Thomas, J. Hallstrom and A. Travesset, *J. Chem. Theory Comput.*, 2024, **20**, 1559–1567.
29 X. Zha and A. Travesset, *J. Phys. Chem. C*, 2018, **122**, 23153–23164.
30 G. Zaldivar, Y. A. Perez Sirkin, G. Debais, M. Fiora, L. L. Missoni, E. Gonzalez Solveyra and M. Tagliazucchi, *ACS Omega*, 2022, **7**, 38109–38121.
31 S. Sadovnikov and A. Gusev, *J. Alloys Compd.*, 2014, **610**, 196–202.
32 Z. I. Zaripov, S. A. Burtsev, A. V. Gavrilov and G. K. Mukhamedzyanov, *Theor. Found. Chem. Eng.*, 2002, **36**, 400–405.
33 P. Pruzan, *J. Chem. Thermodyn.*, 1991, **23**, 247–259.
34 B. W. Goodfellow, M. R. Rasch, C. M. Hessel, R. N. Patel, D.-M. Smilgies and B. A. Korgel, *Nano Lett.*, 2013, **13**, 5710–5714.
35 P. Podsiadlo, B. Lee, V. B. Prakapenka, G. V. Krylova, R. D. Schaller, A. Demortiere and E. V. Shevchenko, *Nano Lett.*, 2011, **11**, 579–588.
36 J. Dymond, K. Young and J. Isdale, *J. Chem. Thermodyn.*, 1979, **11**, 887–895.
37 R. L. Whetten, J. T. Khoury, M. M. Alvarez, S. Murthy, I. Vezmar, Z. L. Wang, P. W. Stephens, C. L. Cleveland, W. D. Luedtke and U. Landman, *Adv. Mater.*, 1996, **8**, 428–433.
38 Z. Fan and M. Grünwald, *J. Am. Chem. Soc.*, 2019, **141**, 1980–1988.
39 K. R. Harris, *J. Chem. Soc., Faraday Trans. 1*, 1982, **78**, 2265.
40 R. Melnyk, I. Nezbeda, D. Henderson and A. Trokhymchuk, *Fluid Phase Equilib.*, 2009, **279**, 1–10.
41 P. J. Camp, *Phys. Rev. E:Stat., Nonlinear, Soft Matter Phys.*, 2003, **67**, 011503.
42 Y. Liu, M. Klement, Y. Wang, Y. Zhong, B. Zhu, J. Chen, M. Engel and X. Ye, *J. Am. Chem. Soc.*, 2021, **143**, 16163–16172.
43 Y. Wang, J. Chen, Y. Zhong, S. Jeong, R. Li and X. Ye, *J. Am. Chem. Soc.*, 2022, **144**, 13538–13546.
44 I. Coropceanu, M. A. Boles and D. V. Talapin, *J. Am. Chem. Soc.*, 2019, **141**, 5728–5740.
45 T. Vo, *Soft Matter*, 2024, **20**, 3554–3576.
46 T. J. Boerner, S. Deems, T. R. Furlani, S. L. Knuth and J. Towns, *Practice and Experience in Advanced Research Computing*, 2023, pp. 173–176.

